eScience 4 (2024) 100208

Contents lists available at ScienceDirect

eScience

journal homepage: www.keaipublishing.com/en/journals/escience

Research Paper

# A plasmonic S-scheme Au/MIL-101(Fe)/BiOBr photocatalyst for efficient synchronous decontamination of Cr(VI) and norfloxacin antibiotic

Shijie Li [a,*], Kexin Dong [a], Mingjie Cai [a], Xinyu Li [a], Xiaobo Chen [b,*]

[a] Zhejiang Key Laboratory of Health Risk Factors for Seafood, National Engineering Research Center for Marine Aquaculture, Zhejiang Ocean University, Zhoushan 316022, China

[b] Department of Chemistry, University of Missouri, Kansas City 64110, USA

## HIGHLIGHTS

- A novel plasmonic MOF-based S-scheme heterostructure of Au/MIL-101(Fe)/BiOBr was devised.
- Au/MIL-101(Fe)/BiOBr exhibited high photo-activity for the eradication of Cr(VI) and norfloxacin.
- Au/MIL-101(Fe)/BiOBr worked more effectively in a Cr(VI)-NOR coexistence system.
- The photocatalysis mechanism, antibiotic degradation pathways, and toxicities were analyzed.
- Integrating MOF-based S-scheme heterojunctions and a plasmonic effect contributed to the reinforced photoactivity.

## GRAPHICAL ABSTRACT

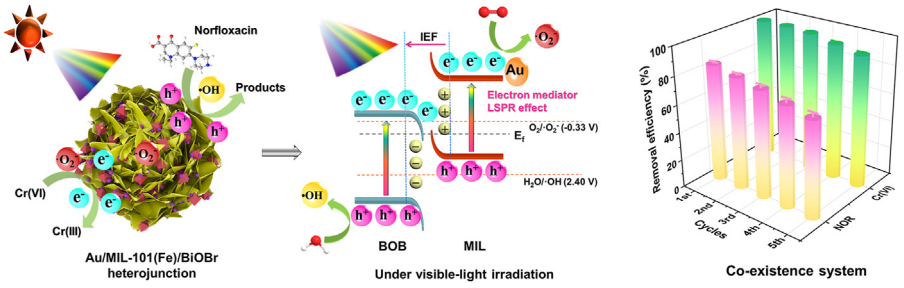


## ARTICLE INFO

*Keywords:*
Au/MIL-101(Fe)/BiOBr
Metal–organic framework (MOF)
Plasmonic effect
S-scheme
Cr(VI) removal
Antibiotic degradation
Synchronous removal

## ABSTRACT

Present photocatalysts for the synchronous cleanup of pharmaceuticals and heavy metals have several drawbacks, including inadequate reactive sites, inefficient electron–hole disassociation, and insufficient oxidation and reduction power. In this research, we sought to address these issues by using a facile solvothermal-photoreduction route to develop an innovative plasmonic S-scheme heterojunction, Au/MIL-101(Fe)/BiOBr. The screened-out Au/MIL-101(Fe)/BiOBr (AMB-2) works in a durable and high-performance manner for both Cr(VI) and norfloxacin (NOR) eradication under visible light, manifesting up to 53.3 and 2 times greater Cr(VI) and NOR abatement rates, respectively, than BiOBr. Remarkably, AMB-2's ability to remove Cr(VI) in a Cr(VI)-NOR coexistence system is appreciably better than in a sole-Cr(VI) environment; the synergy among Cr(VI), NOR, and AMB-2 results in the better utilization of photo-induced carriers, yielding a desirable capacity for decontaminating Cr(VI) and NOR synchronously. The integration of MOF-based S-scheme heterojunctions and a plasmonic effect contributes to markedly reinforced photocatalytic ability by increasing the number of active sites, augmenting the visible-light absorbance, boosting the efficient disassociation and redistribution of powerful photo-carriers, and elevating the generation of reactive substances. We provide details of the photocatalytic mechanism, NOR decomposition process, and bio-toxicity of the intermediates. This synergistic strategy of modifying S-scheme heterojunctions with a noble metal opens new horizons for devising excellent MOF-based photosystems with a plasmonic effect for environment purification.

* Corresponding authors.
*E-mail addresses:* lishijie@zjou.edu.cn (S. Li), chenxiaobo@umkc.edu (X. Chen).

https://doi.org/10.1016/j.esci.2023.100208
Received 29 May 2023; Received in revised form 7 September 2023; Accepted 29 October 2023
Available online 2 November 2023

## 1. Introduction

The issue of water contamination induced by toxic pharmaceuticals and heavy metals is one of the most overwhelming concerns in the area of environmental deterioration, heavily endangering ecological systems and human life [1,2]. To date, numerous means have been extensively applied to address these concerns, such as conventional biodegradation, filtration, electrocatalysis, adsorption, and photocatalysis [3–7]. One of the most economical, effective, and sustainable advanced technologies is sunlight-initiated photocatalysis, which harnesses solar energy to engender powerful radicals that eliminate toxic and recalcitrant pollutants [5,6,8]. However, the photocatalytic destruction of these pollutants commonly encounters difficulties that include weak redox capacity and low catalytic performance, owing to the intrinsic thermodynamic and kinetic sluggishness of the photoreaction [9]. Designing and exploring high-performance sunlight-responsive materials are cornerstone activities in the field of photocatalysis technology [10–22]. It is highly necessary to devise a multifunctional photocatalyst that can achieve the high-efficiency cleanup of toxic pharmaceuticals and metal ions concurrently, due to the widespread co-existence of these contaminants in wastewater.

Among the numerous photocatalysts, BiOBr has aroused significant attention for its admirable layered architecture, high stability, favorable band structure, and remarkable photoelectronic properties [23–25]. Nevertheless, bare BiOBr suffers from a fast photo-carrier reunion rate, limited active sites, and low sunlight harnessing capacity, with unsatisfactory catalytic outcomes [26,27]. To surmount these drawbacks, heterojunction fabrication has proven to be a pragmatic tactic [28–37], with an exceptional S-scheme system gaining increasing interest because of its preeminent photo-carrier reunion suppression and redox potential optimization [38–42]. So far, increasing energy has been devoted to the development of BiOBr-involved S-scheme heterojunctions by combining a variety of non-metal–organic frameworks (non-MOFs) semiconductors (e.g., metal oxides, sulfides, non-metal polymer semiconductors, etc.), and BiOBr [43,44]. However, these non-MOFs/BiOBr S-scheme catalysts have poor reactive sites and other problems that result in unsatisfactory performance.

MOFs have generated tremendous interest in the field of photocatalysis [45–49]; comprising organic molecules and metal ions/clusters, they feature large surface areas, rich and accessible active sites, as well as controllable structure and function. Notably, the promising Fe-based MOF MIL-101(Fe) has been explored as an emerging visible-light-active photocatalyst for wastewater treatment, $CO_2$ reduction, and $H_2$ production because of its amazing structural merits, unique ligand-metal charge migration route, and suitable band structure [50,51]. Recent works have shown that MIF-101(Fe) can function as an efficient co-catalyst, and that designed MIF-101(Fe)-based systems have the advantages of sufficient surface-exposed reactive sites and improved photo-carrier shuttling, boosting the material's catalytic properties [52–54]. Significantly, the localized surface plasmon resonance (LSPR) of noble metals can be utilized to foster the detachment and transport of photo-carriers and reinforce sunlight absorption by the heterostructure. Typically, Au with LSPR is developed as a classic plasmonic material to boost the photoreaction kinetics [55–58]. Building a plasmonic MOF-based S-scheme heterojunction that can integrate the merits of a plasmonic effect, a MOF, and an S-scheme architecture is therefore a prospective strategy for obtaining high-performance photocatalysts for environmental purification. Yet no research on the development of plasmonic S-scheme photocatalysts based on MIL-101(Fe) for wastewater contamination has hitherto been reported.

Based on the foregoing, we developed an innovative plasmonic heterostructure of Au/MIL-101(Fe)/BiOBr through combining the superior qualities of a MOF-based S-scheme heterostructure and plasmonic Au. The establishment of a LSPR-assisted MOF-involved S-scheme configuration resulted in a broader light absorption range, stronger photoredox capacity, and plenty of exposed reaction sites, enabling Au/MIL-101(Fe)/BiOBr to achieve superior photo-redox ability for the synchronous destruction of antibiotics and Cr(VI). This research provides a strategy to develop a plasmonic photocatalyst combining a MOF-containing S-scheme heterostructure for the photocatalytic eradication of antibiotics and Cr(VI) simultaneously.

## 2. Experiment

### 2.1. Sample synthesis

The synthesis process of Au/MIL-101(Fe)/BiOBr (AMB) is summarized in Fig. 1a.

#### 2.1.1. Synthesis of MIL-101(Fe) (MIL)

MIL-101(Fe) crystals were synthesized through a solvothermal approach [52]. 1 mmol each of $H_2BDC$ and $FeCl_3{\cdot}6H_2O$ were separately dissolved in 18 mL of DMF using ultrasonication for 20 min. Next, under constant stirring, the $H_2BDC$ solution was mixed with the $FeCl_3$ solution. After further agitation for 60 min, the reaction precursors were injected into a 50 mL autoclave in an oven at 110 °C for 20 h to finish the reaction. The MIL solids were washed with hot DMF and ethanol, then dried at 70 °C in a vacuum oven overnight.

#### 2.1.2. Synthesis of MIL-101(Fe)/BiOBr (MIL/BOB)

Typically, 1.0 mmol of $Bi(NO_3)_3{\cdot}5H_2O$ was dissolved in 12 mL of ethylene glycol with sonication for 30 min. Next, 0.092 g of MIL was introduced into the $Bi(NO_3)_3$ solution with agitation for 1 h. After that, KBr solution obtained by dissolving KBr (1.0 mmol) into ethanol (12 mL) and ethylene glycol (12 mL) was injected dropwise into the above suspension with constant agitation for 2 h. After that, the obtained solution was sealed in a 50 mL autoclave and reacted at 140 °C for 10 h. Once the reaction mixture had cooled down, MIL/BOB was obtained after being washed three times with ethanol and water. Using the same method, BiOBr was also prepared in the absence of MIL.

#### 2.1.3. Au/MIL-101(Fe)/BiOBr (AMB)

AMB heterojunctions were fabricated via a facile photoreduction approach. 0.5 g of MIL/BOB and a certain amount of $HAuCl_4$ were dispersed in 30 mL of methanol and 20 mL of $H_2O$ with constant agitation for 30 min. Next, the mixture underwent illumination with a 300 W xenon lamp for 30 min. AMB heterojunctions with 0.5, 1, and 3 wt% of Au (denoted as AMB-1, AMB-2, and AMB-3) were attained through washing, centrifugation, and drying.

### 2.2. Photo-activity assessment

Experiments assessing the photocatalytic eradication of Cr(VI) and NOR were conducted under visible light to appraise the catalytic ability of the as-built nanomaterials. The photoreactions were carried out in a glass reactor (250 mL) at 25 ± 2 °C. Before illumination, 40 mg of the nanomaterial were dispersed in the Cr(VI) (20 mg/L, 150 mL) or NOR (10 mg/L, 150 mL) solutions, then the reaction suspensions underwent sonication for 20 s and agitation for 30 min. Next, the lamp ($\lambda > 420$ nm, 300 W Xe lamp) was turned on to illuminate the continuously stirred reaction system, triggering the reaction. 1.0 mL of specimen was extracted at certain intervals, and its concentration was determined by a UV–vis spectrometer, wherein the Cr(VI) concentration was monitored according to the standard diphenylcarbazide (DPC) approach. All the experiments were completed in triplicate.

## 3. Results and discussion

### 3.1. Composition and morphology

Scanning electron microscopy (SEM) and transmission electron microscopy (TEM) characterizations were conducted to disclose the microstructures of BOB and AMB-2. BOB presents a nanoflower architecture built from stacked nanoplates with tidy surfaces (Fig. 1b). The as-built

AMB-2 possesses a similar nanoflower-shaped structure, and its surface is tightly covered with MIL octahedrons (size: ~100–700 nm) and Au NPs (size: ~5–30 nm) (Figs. 1c–e). The densely connected interface of AMB-2 is an advantageous morphological configuration for the interfacial transportation and separation of photo-created charge carriers during the photoreaction, boosting ROS generation [39,59] (Figs. 1c–g). High-resolution TEM (HR-TEM) reveals a pronounced lattice spacing of 0.28 nm, equivalent to the (012) crystal plane of BOB (Fig. 1h), which is consistent with the X-ray diffraction (XRD) analysis (Fig. 2a). The Energy-dispersive X-ray (EDX) spectrum and elemental mapping (Fig. 1i) also corroborate the presence of Fe, C, Au, O, Br, and Bi elements and the even dispersion of Fe, C, and Au on the entire nanoflower, signifying the successful fabrication of AMB-2.

The phase structures of BOB, MIL, MIL/BOB, AMB-1, AMB-2, and AMB-3 were identified via powder XRD (PXRD) analysis (Fig. 2a). All the diffraction peaks of BOB and MIL are consistent with BiOBr (JCPDS 73–2061) [28] and MIL-101(Fe) [50], respectively. The as-built MIL/BOB unveils the characteristic peaks of BOB, with weakened crystallinity; no MIL signals are apparent, probably due to the small amount and low crystallinity of MIL in the heterojunction. With decoration by Au NPs, all the AMB heterojunctions exhibit PXRD patterns similar to that of MIL/BOB, ascribed to the small amount of Au NPs. To confirm the formation of the AMB heterostructure, Fourier transform infrared (FT-IR) and X-ray photoelectron spectroscopy (XPS) characterizations were performed.

The surface chemical components of MIL, BOB, and AMB-2 were examined by FT-IR (Fig. S1a). The FT-IR spectrum of BOB contains a characteristic peak centered at 501.49 $cm^{-1}$, assigned to the Bi–O bond. In the case of MIL, the distinct bands at 547.78 and 749.16 $cm^{-1}$ are from Fe–O vibration modes [60]. The bands at 1396.51, 1597.06, and 1658.81 $cm^{-1}$ correspond to the O–C=O group of $H_2BDC$ [61]. The FT-IR spectrum of AMB-2 presents the typical peaks of MIL and BOB, with slight shifts, indicating MIL and BOB are well combined in AMB-2. No Au band is visible due to the low Au content.

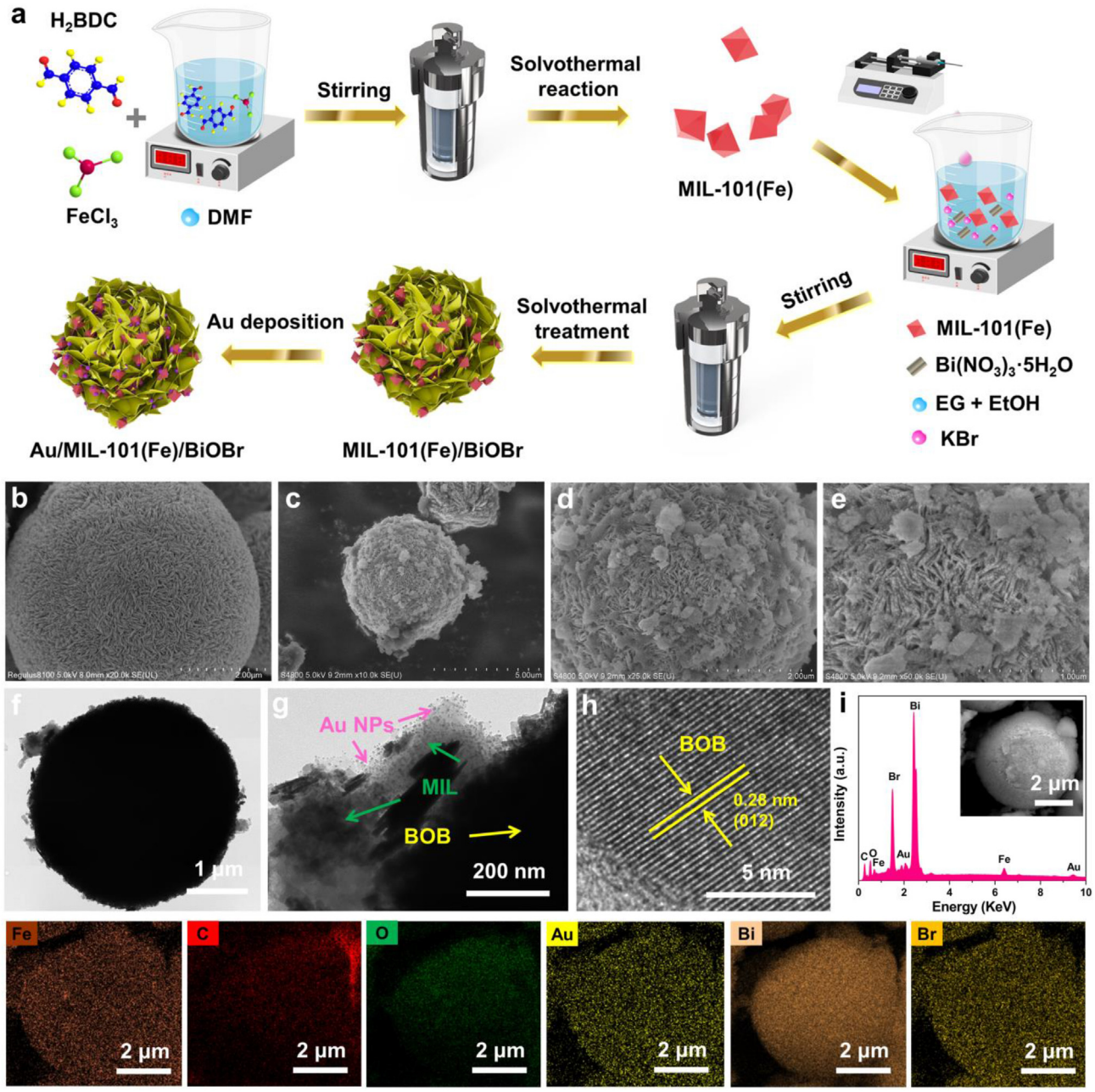


**Fig. 1.** (a) Illustration of the AMB catalyst fabrication process; (b) SEM image of BOB; (c–e) SEM images of AMB-2; (f, g) TEM images, (h) HR-TEM image, (i) EDX and elemental mapping images of AMB-2.

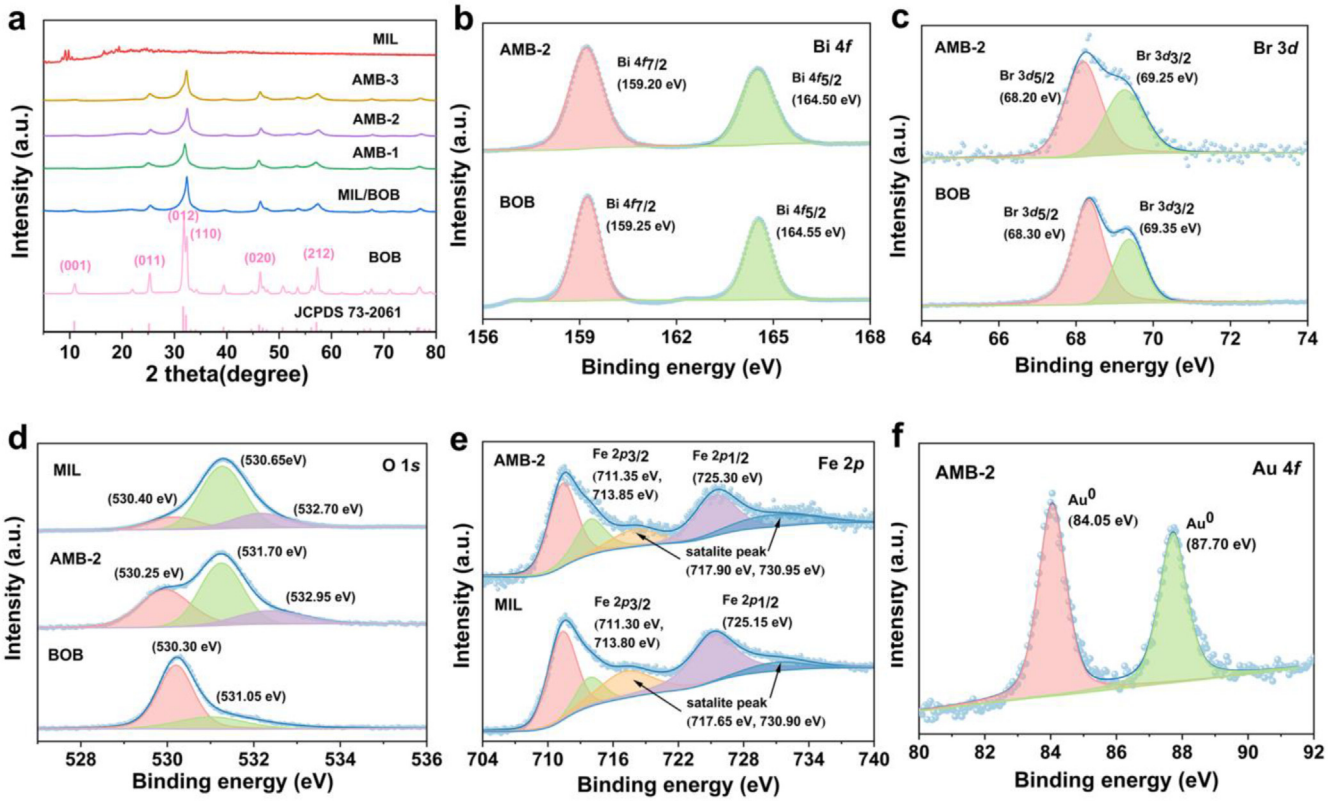


**Fig. 2.** (a) PXRD patterns of as-built catalysts; XPS spectra of (b) Bi 4f, (c) Br 3d, (d) O 1s, (e) Fe 2p, (f) Au 4f of BOB, MIL, and AMB-2.

The chemical states of the catalysts were studied with XPS (Figs. 2b–f and Figs. S1b and c). The survey spectrum in Fig. S1b indicates AMB-2 contains Bi, C, O, Fe, and Br elements, confirming the perfect integration of MIL, Au, and BOB. Figs. 2b and c display the Bi 4f and Br 3d spectra. The peaks at 164.55 and 159.25 eV are from Bi $4f_{5/2}$ and Bi $4f_{7/2}$, respectively (Fig. 2b) [62], and the signals at 69.35 and 68.3 eV belong respectively to Br $4f_{3/2}$ and Br $4f_{5/2}$ (Fig. 2c) [28], which can be credited to the $Bi^{3+}$ and $Br^{-}$ in BOB. In Fig. 2d, the O 1s spectrum of BOB unveils two signals at 530.3 and 531.05 eV, in accordance with the lattice O atom and the attached O surface group. The Fe 2p spectrum of MIL is divided into five peaks: Fe $2p_{3/2}$ (711.3 and 713.8 eV), Fe $2p_{1/2}$ (725.15 eV), and the satellite peaks (730.9 and 717.65 eV), signifying the presence of $Fe^{3+}$ and $Fe^{2+}$ in MIL (Fig. 2e) [52]. The Au spectrum of AMB-2 contains two prominent signals at 84.05 and 87.7 eV, assigned to Au 4f (Fig. 2f) [55]. The C 1s spectrum of AMB-2 presents three typical signals, corresponding to the C–C (284.8 eV), C–O (286.25 eV), and O–C=O (288.8 eV) bonds (Fig. S1c). Notably, the binding energies (BEs) of Bi and Br (Fe and O) in AMB-2 become more negative (positive) in comparison with those in single BOB (MIL), indicating the electrons of MIL jump into BOB across the heterointerface. Such electron acceptor–donor coupling between BOB and MIL gives rise to an internal field from MIL to BOB.

The Brunauer–Emmett–Teller (BET) surface area information for BOB, MIL, and AMB-2 were acquired by measuring $N_2$ adsorption–desorption curves (Fig. S2). Benefiting from its highly porous architecture, MIL has an impressive specific surface area (362.17 $m^2/g$). After incorporating MIL-101(Fe), BiOBr, and Au, the as-built AMB-2 demonstrates a substantial improvement in surface area (241.13 $m^2/g$) relative to pristine BiOBr (10.2 $m^2/g$), which boosts sunlight-driven photo-redox reactions by supplying numerous pollutant-capturing and reaction sites [62–64].

### 3.2. Photocatalytic performance

Photocatalytic Cr(VI) reduction tests were implemented over as-built materials under visible light (Fig. 3a and Fig. S3a). As depicted in Fig. 3a, compared with bare BOB, the binary and ternary heterojunctions possess reinforced Cr(VI) adsorption capacity, which is associated with the incorporation of porous MIL. The photocatalytic Cr(VI) reduction capabilities of the as-built materials are in the order AMB-2 (99.1%) > AMB-3 (93.4%) > AMB-1 (75.9%) > MIL/BOB (55.9%) > MIL (35.8%) > BOB (10.7%). Significantly, the binary MIL/BOB outperforms the pristine samples, due to the production of favorable S-scheme junctions. Thanks to the synergy of the LSPR effect between the Au and the S-scheme architecture, the as-built AMB heterojunctions obtain reinforced photo-activity compared to MIL/BOB. The photoreduction activity of AMB is associated with various Au contents because of different functions: suitable Au content can take full advantage of the LSPR effect in the AMB heterojunction, while superfluous Au can cover the reactive centers and block visible-light utilization [56]. Impressively, AMB-2 loaded with the proper dose of Au has maximum Cr(VI) eradication activity. The Cr(VI) abatement rate constants were determined through fitting the pseudo-first-order kinetics (Fig. S3a). AMB-2 achieves the largest rate constant of 0.2337 $min^{-1}$, which is 18.3, 53.3, and 5.2 times more than for MIL (0.0121 $min^{-1}$), BOB (0.0043 $min^{-1}$), and MIL/BOB (0.0375 $min^{-1}$), respectively.

The photocatalytic Cr(VI) abatement efficiency of AMB-2 at different pH values was assessed. As shown in Fig. 3b, after 20 min of reaction, 100%, 100%, 99.1%, 67.8%, and 45.4% of Cr(VI) was eliminated by AMB-2 at pH levels of 2.5, 4.0, 5.5, 7.0, and 8.5, respectively. Notably, AMB-2 is capable of effectively photo-reducing Cr(VI) at low pH, indicating acidic conditions are helpful for Cr(VI) reduction over AMB-2, because abundant $H^+$ accelerates the reduction of Cr(VI) into Cr(III) [39,50]. The attenuated activity under alkaline conditions could result from the lack of $H^+$ [39].

The Cr(VI) photoreduction ability of AMB-2 with organic acids was also evaluated (Fig. S3b). It is clear that the photo-activity of AMB-2 is significantly upgraded after the injection of organic acids, as they make a significant contribution to enriching the photo-induced electrons by capturing photo-produced holes. Among these acids, tartaric acid plays

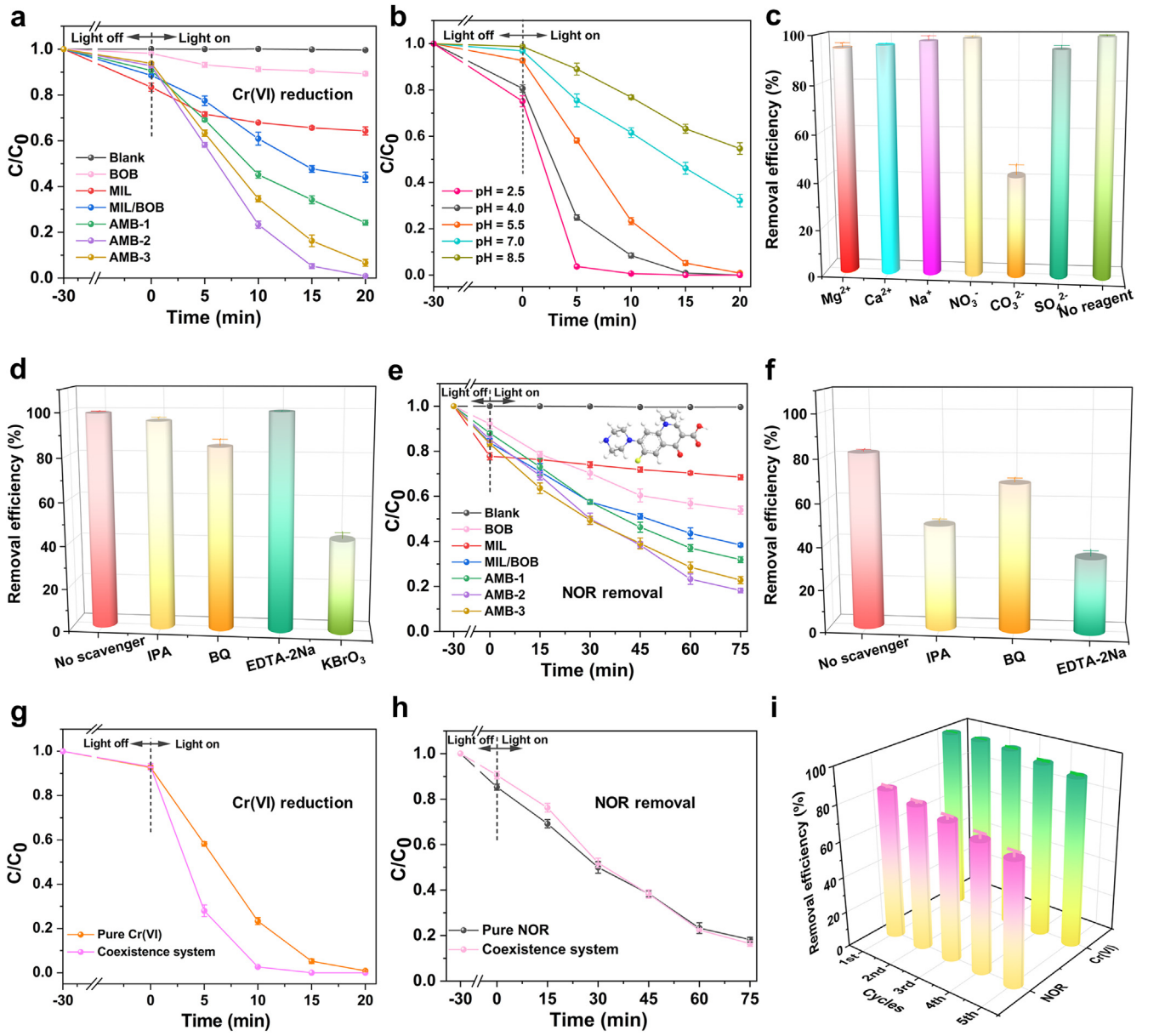


**Fig. 3.** (a) Photocatalytic Cr(VI) abatement over as-built samples across time; (b) capability of AMB-2 to eliminate Cr(VI) at different pH levels; (c) effects of various salts on Cr(VI) eradication efficiency over AMB-2; (d) capability of AMB-2 to eliminate Cr(VI) with quenchers present; (e) photocatalytic NOR destruction over as-built samples across time; (f) ability of AMB-2 to eliminate NOR with quenchers present; capability of AMB-2 to eliminate Cr(VI) (g) and NOR (h) in a co-existence system and a sole-pollutant system; (i) stability of AMB-2 when eliminating Cr(VI) and NOR simultaneously.

the most significant role in boosting Cr(VI) removal (Fig. S3b), due to the number of α-hydroxyl groups it contains.

The Cr(VI) photoreduction performance of AMB-2 in coexistence with different anions was examined. Fig. 3c shows that all the anions except for $CO_3^{2-}$ have a negligible impact on Cr(VI) abatement, but in the presence of $CO_3^{2-}$, Cr(VI) abatement is notably inhibited, with 56.8% activity loss due to the elevated pH induced by $CO_3^{2-}$.

To assess AMB-2's applicability under real-world conditions, its photo-activity for Cr(VI) abatement in tap water and river water was tested. As exhibited in Fig. S3c, the photo-activity of AMB-2 is inhibited to a moderate extent in both water matrices, with 95.8% and 82.7% Cr(VI) removal in river and tap water, respectively. The moderate activity decrease is credited to the presence of organics and inorganics, which result in fewer exposed reactive centers and/or less visible-light absorption [62]. The above findings reflect the significant potential of AMB-2 for actual implementation.

Radical-capturing experiments were implemented to identify the reactive species responsible for Cr (VI) eradication. As depicted in Fig. 3d, the injection of benzoquinone (BQ, quencher of $\cdot O_2^-$) brings about a certain inhibitory effect on Cr(VI) eradication, reflecting that $\cdot O_2^-$ species are involved in the photoreaction. The abatement of Cr(VI) is considerably suppressed in the presence of $KBrO_3$ (quencher of $e^-$), substantiating the prominent role of $e^-$ in the photocatalytic Cr(VI) eradication process (Fig. 3d).

The performance of BOB, MIL, MIL/BOB, AMB-1, AMB-2, and AMB-3 for the photocatalytic NOR destruction reaction was also evaluated (Fig. 3e), and we found that the AMB ternary heterojunctions outperform the original materials and the binary heterojunction. The best-performing AMB-2 had a NOR degradation efficiency of up to 81.8% within 75 min. Impressively, the rate constant of AMB-2 reached 0.0214 $min^{-1}$, which was 2.0, 11.6, and 1.1 times higher than that of BOB (0.0072 $min^{-1}$), MIL (0.0017 $min^{-1}$), and MIL/BOB (0.0104 $min^{-1}$) (Fig. S4a).

The photocatalytic NOR eradication performance of AMB-2 under real environmental conditions was also examined. Fig. S4b shows the eradication efficiency of NOR dropping by 2.9% and 13% in tap water and river water, respectively, due to interference from organic and inorganic substances [38]. However, the inhibitory impact is limited, confirming the remarkable application potential of AMB-2. More significantly, AMB-2 also manifests robust treatment efficacy towards the destruction of oxytetracycline (85.2%, 90 min) and ciprofloxacin (91.6 %, 75 min) (Fig. S4c). The radical-quenching test was performed to determine the role of ROS (Fig. 3f). With the injection of BQ, IPA, and EDTA-2Na, the NOR abatement rates drop by 13.2%, 32.7%, and 46.6%, respectively, revealing the pivotal role of $h^+$ and ·OH for NOR destruction.

The coexistence of toxic metals (e.g., Cr(VI)) and antibiotics (e.g., NOR) in wastewater poses the challenge of effectively eradicating these pollutants. Thus, tests were conducted in a Cr(VI)-NOR environment to check the potential of AMB-2 for their concurrent cleanup. From Fig. 3g, we can see that the Cr(VI) abatement efficiency over AMB-2 rises to 100 % within 15 min in the Cr(VI)-NOR mixed environment, and the corresponding k is as high as 0.3556 $min^{-1}$, about 1.5 times that achieved in a pure Cr(VI) environment (Fig. S5a). Evidently, the catalytic Cr(VI) abatement ability of AMB-2 is substantially strengthened in a Cr(VI)-NOR mixed environment compared with in a pure Cr(VI) solution. This results from the synergy between the plasmonic S-scheme catalyst, Cr(VI), and NOR, wherein the NOR scavenges photo-induced $h^+$ in AMB-2, ensuring the effective detachment and enrichment of $e^-$ for the photoreduction of Cr(VI) [65,66]. AMB-2 also maintains high activity towards NOR eradication in this co-existence environment (Fig. 3h and Fig. S5b). Overall, AMB-2 is capable of synchronously eliminating Cr(VI) and NOR in effluent, due to the creation of a special LSPR coupling S-scheme architecture that ensures the concurrent utilization of photo-created electrons and holes.

The mineralization activity of AMB-2 was evaluated by detecting the total organic carbon (TOC) values of NOR wastewater before and after treatment (Fig. S6). After 75 min of photoreaction, AMB-2 achieved 40.1 % TOC abatement, signifying it has notable mineralization performance.

Stability is an important index for evaluating the sustainability and practicality of photocatalysts for wastewater purification. Thus, the photocatalytic stability of AMB-2 in a co-existence system was checked through five successive cycles. We see in Fig. 3i that the removal efficiencies of Cr(VI) and NOR are diminished by only 6.9 % and 14.9 % after the fifth cycle, reflecting the AMB-2's high recycling stability. Moreover, the FT-IR spectrum, XRD pattern, and XPS spectra (Bi 4f, Br 3d, and Fe 2p) of the used AMB-2 after tests are similar to those of the original (Figs. S7a–e), verifying its structural stability. XPS measurement was also conducted to reveal the photoreduction product of Cr(VI) over AMB-2 (Fig. S7f). The XPS spectrum of Cr 2p contains two typical signals of Cr(III): 577.87 eV (Cr $2p_{3/2}$) and 587.34 eV (Cr $2p_{1/2}$). This finding demonstrates the photocatalytic conversion of Cr(VI) to Cr(III) in the AMB-2/visible-light system [62].

To illustrate the process of NOR degradation by AMB-2, we used liquid chromatography–mass spectrometry to identify intermediates, sampling the reaction solution at various times (Fig. S8, Table S1). On the basis of the *m/z* values, the molecular structures of the intermediates were identified and are displayed in Table S1. Basically, the degradation process of NOR over AMB-2 consists mainly of functional group detachment (e.g., defluorination, decarboxylation, etc.), ring opening, bond cleavage, and deep oxidation. To be specific, two photocatalytic NOR transformation routes are proposed (Fig. 4a). In route I, the assault of ROSs and $h^+$ on the NOR breaks the piperazine ring, engendering P1 ($m/z = 294$). Next, C–N bond breakage occurs, decomposing P1 into P2 ($m/z = 252$). After that, defluorination, decarboxylation, and pyridine ring breakage bring about the transformation of P2 into P3 ($m/z = 148$). In route II, the generation of P4 ($m/z = 259$) from NOR is achieved through defluorination and the opening of piperazine rings. Next, P4 ($m/z = 259$) is oxidized into P5 ($m/z = 292$), which is further decomposed into P6 ($m/z = 171$) and P7 ($m/z = 121$) via decarboxylation, deamination, and bond-cleavage reactions. The fierce, deep oxidation reactions bring about the fragmentation of aromatic moieties and cyclic structures, resulting in the low-molecular-weight compounds of P8–P11.

The toxicity of NOR and the byproducts of its breakdown were estimated by utilizing T.E.S.T. software (Figs. 4b–d and Table S2). The majority of the intermediates show distinctly lower acute toxicity than NOR (Fig. 4b). NOR's mutagenicity value (0.6) is higher than most of the byproducts' values, with P7 (−0.01) and P9 (0.5) being mutagenically negative compounds (Fig. 4c). Most of the byproducts exhibit decreased developmental toxicity compared to NOR, except P1, P4, and P5, with P3, P7, P9, and P11 being developmental non-toxicants (Fig. 4d). The above findings signify that treatment by the AMB-2 photosystem could effectively lessen the overall eco-toxicity of a NOR solution, implying that AMB-2 holds promise for the practical treatment of antibiotic wastewater.

As we know, light responsiveness is a fundamental prerequisite for photocatalysts to initiate photoreactions. Thus, the absorption spectra of BOB, MIL, MIL/BOB, AMB-1, AMB-2, and AMB-3 were measured and presented in Fig. 5a. BOB and MIL can harvest UV light and visible light below ≈ 470 and 526 nm, in accordance with bandgaps ($E_g$) of 2.63 and 2.15 eV, obtained utilizing the Kubelka−Munk function: $(\alpha hv)^2 = A(hv - E_g)$ (Fig. 5b). MIL/BOB has demonstrably better light-capturing ability compared to BOB and MIL on their own, which is attributed to the MIL/BOB heterojunction. Encouragingly, the AMB-1, AMB-2, and AMB-3 ternary heterojunctions manifest appreciably better spectral absorption from 200 to 800 nm, benefiting from the LSPR absorption of Au NPs, which concurs with previous findings [55]. This fact indicates that AMB heterojunctions can effectively take advantage of visible light to drive photoreactions.

The Mott−Schottky profiles of MIL and BOB were acquired to define their conduction band (CB) potentials (Fig. 5c) [67]. The flat-band positions ($E_{fb}$) of MIL and BOB are about −0.82 and −0.47 V versus Ag/AgCl, equal to −0.62 and −0.27 V versus NHE. Given the $E_{CB}$ is approximately 0.1 V more negative than the $E_{fb}$ in n-type semiconductors, the $E_{CB}$ of MIL and BOB are −0.72 and −0.37 V (versus NHE), revealing the CB electrons of both components are energetically capable of triggering the conversion of $O_2$ to $\cdot O_2^-$ species. On the basis of the defined $E_g$ from the DRS spectra and the equation $E_{CB} = E_{VB} - E_g$, the $E_{VB}$ of MIL and BOB would occur at 1.43 and 2.26 V (versus NHE), revealing the sufficient oxidative potential of the BOB VB holes for accomplishing the formation of ·OH from $OH^-$. The corresponding energy diagram of AMB is depicted in Fig. 5f.

To observe the charge transport behavior at the hetero-interface, we used ultraviolet photoelectron spectroscopy (UPS) to define the work function (Φ) of BOB (5.52 eV) and MIL (4.55 eV) (Fig. 5d). Valence band (VB) XPS was employed to define the Fermi level ($E_f$) of BOB (0.79 V) and MIL (−0.53 V) (Fig. 5e). The large Φ ($E_f$) variation between MIL and BOB is conducive to the acquisition and redistribution of directed charge flow so as to trigger an attractive internal electric field (IEF) from MIL to BOB and edge bending upon their hybridization (Fig. 5j), fostering the enrichment and utilization of photo-induced carriers for ROS generation during photocatalysis.

To obtain significant evidence for the S-scheme charge transport path during photocatalysis, we implemented in situ irradiated XPS measurement [38,68]. Under light illumination, the Bi 4f and Br 3d peaks move to higher BEs, while the Fe 2p peak shifts to a lower BE (Figs. 5g–i). The above phenomenon reveals the directional movement of photo-induced electrons from BOB to MIL under light illumination, confirming the fabrication of an S-scheme junction between them.

Evidently, upon the creation of AMB-2 in darkness (Fig. 5j), the electrons ($e^-$) of MIL spontaneously jump into BOB to equilibrate their $E_f$ levels, giving rise to an IEF from MIL to BOB and upward (downward) band-bending of MIL (BOB), consistent with the XPS findings (Figs. 2b–f) and work function determination (Fig. 5d). When irradiated by light, the photo-induced electrons of BOB preferably transfer to MIL and

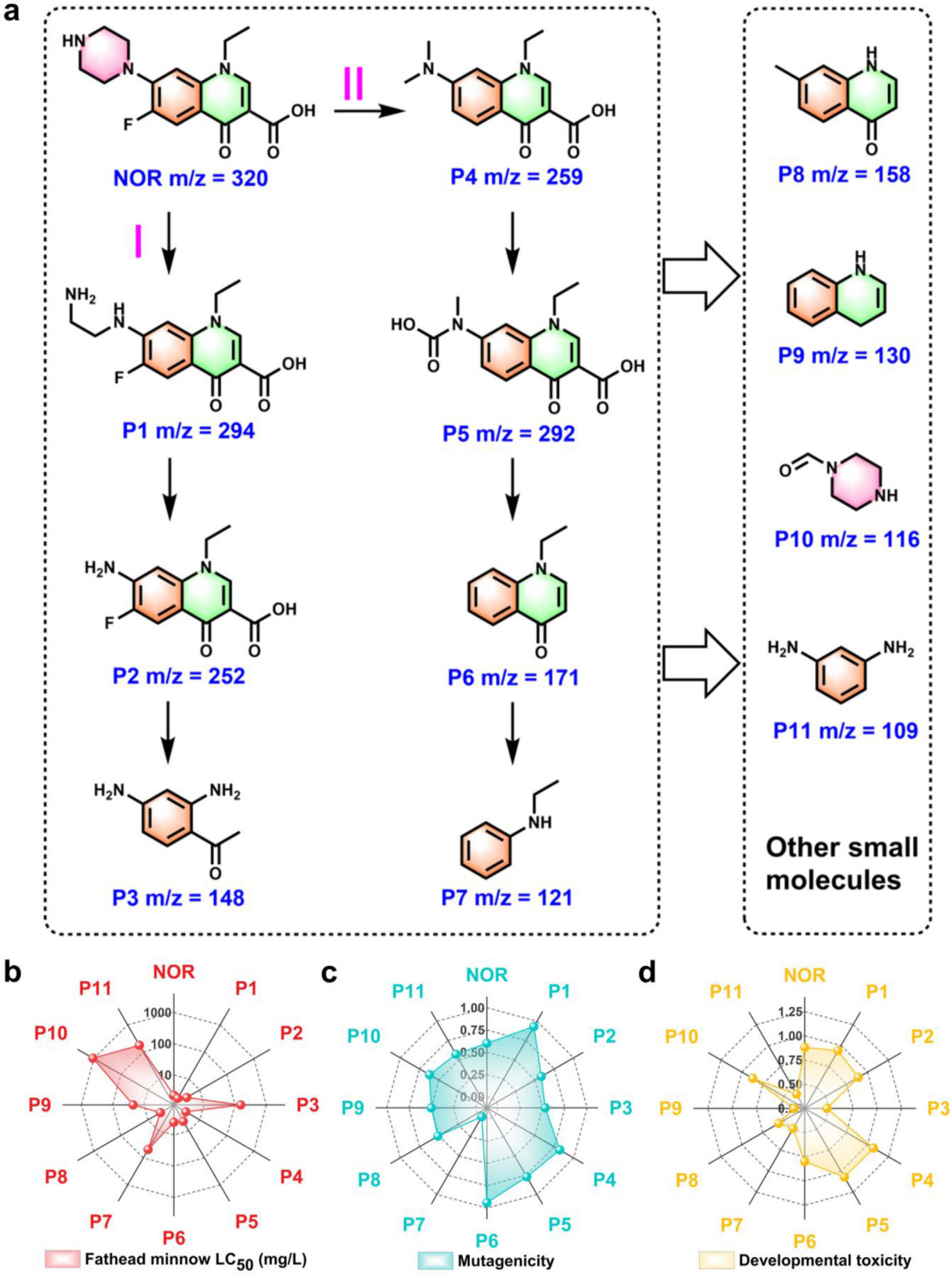


**Fig. 4.** (a) Photocatalytic NOR transformation process over AMB-2; (b–d) Eco-toxicity assessment.

recombine with the VB holes of MIL (Figs. 5g–i), contributing to the effective storage of powerful carriers for ROS generation.

Photo/electrochemical measurements were performed to elucidate the photo-created carrier dynamics of BOB, MIL, MIL/BOB, and AMB-2. The transient photocurrent responses under chopped light irradiation for five cycles are presented in Fig. 6a. AMB-2 exhibits a substantially stronger TPR signal than BOB, MIL, and MIL/BOB, implying the effective reinforcement of the photo-carrier concentration induced by the

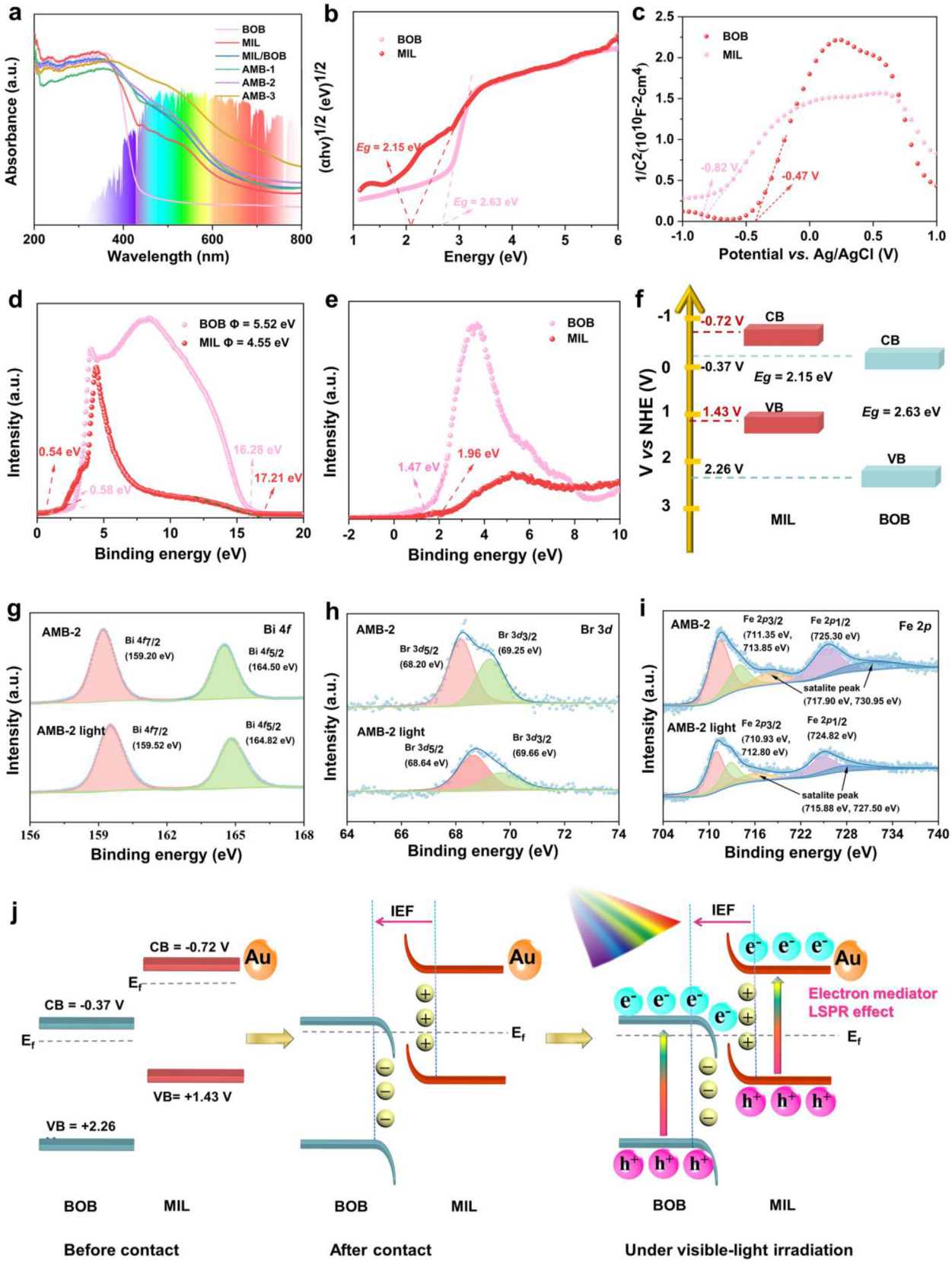


**Fig. 5.** (a) UV–vis spectra of as-built catalysts; (b) Tauc's profiles, (c) Mott–Schottky profiles, (d) UPS spectra, and (e) VB-XPS spectra of BOB and MIL; (f) electronic band alignment of MIL/BOB; XPS spectra of (g) Bi 4f, (h) Br 3d, and (i) Fe 2p for BOB, MIL, and AMB-2 in darkness and under illumination; (j) illustration of the S-scheme electron migration mechanism in the AMB-2 heterojunction.

plasmonic S-scheme heterojunction. Electrochemical impedance spectroscopy (EIS) was applied to define the charge transportation impedance of the as-built catalysts (Fig. 6b). The equivalent circuit for the system is presented in the inset of Fig. 6b. In this model, $R_1$, $R_2$, $W_1$, and $C_2$ respectively represent the resistance between the fluorine-doped tin oxide and catalysts, the charge migration resistance across the photoanode/electrolyte interface, the Warburg impedance, and the constant phase element, which are provided in Table S3. Basically, the smaller the arc radius, the faster the charge migration rate [62,69,70]. Notably, AMB-2 manifests a considerably smaller arc radius and lower $R_2$ of 71,

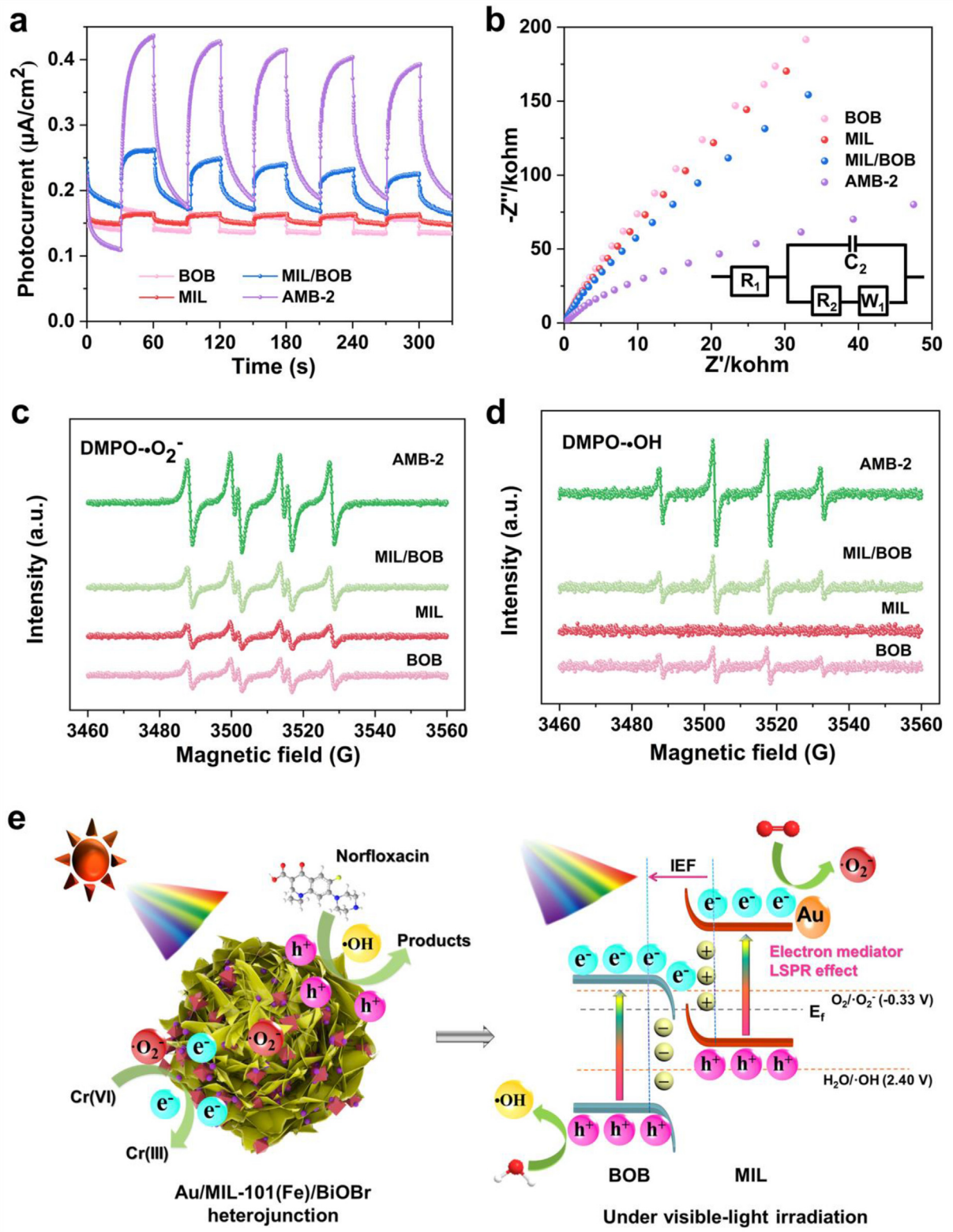


**Fig. 6.** (a) Transient photocurrent intensity and (b) EIS plots of as-built materials; (c, d) ESR identification of $\cdot O_2^-$ and ·OH production over MIL, BOB, MIL/BOB, and AMB-2 under illumination; (e) mechanism of photocatalytic Cr(VI)/NOR eradication over the AMB catalyst.

122 Ω compared with BOB ($R_2$, 1,489,000 Ω), MIL ($R_2$, 561,370 Ω), and MIL/BOB ($R_2$, 500,060 Ω), meaning a considerable enhancement of photo-carrier transport and separation performance. The photoluminescence (PL) spectra were acquired to appraise the detachment capacity of photo-excited carriers (Fig. S9). It is widely recognized that fast carrier reunion triggers the increments in a PL signal [62]. As shown in Fig. S9, BOB possesses the strongest PL intensity, signifying rapid photo-carrier reintegration. The PL intensity of binary MIL/BOB is quenched, reflecting the optimization of charge dissociation. After integrating Au and MIL/BOB, the resulting AMB-2 affords the weakest PL intensity, verifying the advantages of AMB-2 for accelerating the photo-carrier detachment and transportation processes. The above findings prove that the plasmonic S-scheme configuration of AMB-2 is helpful for efficiently disintegrating photo-induced carriers, thus promoting the photocatalytic outcome.

The electron spin resonance (ESR) spectra of MIL, BOB, MIL/BOB and AMB-2 were examined to assess the ROS ($\cdot O_2^-$ and ·OH) production performance (Figs. 6c and d). Specifically, the $\cdot O_2^-$ signal can be seen in MIL, BOB, MIL/BOB, and AMB-2 under light irradiation. Among them, the $\cdot O_2^-$ signal intensity of AMB-2 is substantially reinforced compared to MIL/BOB, MIL, and BOB (Fig. 6c), indicating the advantage of AMB-2 for producing $\cdot O_2^-$ species. With respect to the ·OH signal, MIL exhibits no ·OH signal, because the VB $h^+$ of MIL is too negative to form ·OH radicals. Strikingly, AMB-2 also demonstrates superior ability in the photocatalytic generation of ·OH compared with MIL/BOB, MIL, and BOB (Fig. 6d), implying that the plasmonic S-scheme architecture encourages the formation of $\cdot O_2^-$ and ·OH radicals. The ESR findings are in agreement with the XPS results, work functions, and Fermi levels, corroborating the formation of the plasmonic S-scheme heterojunction.

Drawing upon the above discussions, the plasmonic effect-assisted S-scheme photocatalysis mechanism of AMB-2 is illustrated in Fig. 6e. Under illumination, the electrons in both BOB and MIL are photoproduced from their VB to their CB, where this process in MIL is achieved via a ligand-to-metal charge transfer (LMCT) route that is a general photoexcitation manifold among coordination compounds of transition metals with an empty valence shell [71]. Subsequently, the IEF and bandbending make it easier for the photo-induced electrons of BOB to reintegrate with the holes of MIL, achieving the fast eradication of weak carriers and the effective separation and enrichment of energetic carriers for photocatalysis [38,40]. Beyond that, the LSPR effect of Au greatly reinforces the photocatalytic outcome through the injection of LSPR-generated hot electrons into MIL and boosts the responsiveness to sunlight, thus promoting the photoreactions [72,73].

Notably, although significant progress has been made in the field of S-scheme systems, a plasmonic MOF-based S-scheme architecture with strong interfacial connections has rarely been developed for the synchronous cleanup of antibiotics and Cr(VI). Overall, the creation of the LSPR effect combining MOF-based S-scheme heterojunctions, characteristics of reinforced visible-light harnessing capacity, optimal photoredox potential, and the availability of numerous exposed reactive centers promotes the effective production of abundant reactive species for the highly efficient eradication of Cr(VI) and NOR simultaneously. The main photoreactions for Cr(VI) and NOR cleanup are as follows:

$$\mathrm{AMB}+h\nu \rightarrow \mathrm{AMB}(e^-, h^+) \quad (1)$$

$$h^+(\mathrm{MIL}) + e^-(\mathrm{BOB}) \rightarrow \text{reintegration} \quad (2)$$

$$e^-(\text{MIL and Au}) + O_2 \rightarrow \cdot O_2^- \quad (3)$$

$$h^+\ (\mathrm{BOB}) + H_2O \rightarrow \cdot OH + H^+ \quad (4)$$

$$\cdot OH/h^+ + \mathrm{NOR} \rightarrow CO_2 + H_2O + \text{small molecules} \quad (5)$$

$$\cdot O_2^-/e^- + \mathrm{Cr(VI)} \rightarrow \mathrm{Cr(III)} \quad (6)$$

## 4. Conclusions

In conclusion, we have developed a plasmonic coupling architecture of Au/MIL-101(Fe)/BiOBr (AMB-2) via a facile route. The AMB-2 catalyst integrates a MOF-involved S-scheme junction with the local surface plasmon resonance excitation of Au nanoparticles, which not only yields ample reaction sites but also upgrades the light-capturing capability and promotes the disassociation of charge carriers. AMB-2 demonstrates a distinctive photo-redox activity against Cr(VI) and NOR, surpassing the activity of MIL, BOB, and MIL/BOB. Significantly, AMB-2 is capable of effectively accomplishing the synchronous decontamination of Cr(VI) and NOR. More impressively, the AMB-2 system manifests excellent potential for treating actual wastewater. This work provides new insights for the exploration of novel plasmonic coupling MOF-based S-scheme photocatalysts based on cooperative photo-redox systems for sustainable environmental remediation.

## Author contributions

**Shijie Li:** Conceptualization, Project administration, Supervision, Writing – original draft, Writing – review & editing. **Kexin Dong:** Data curation, Formal analysis, Investigation, Methodology. **Mingjie Cai:** Data curation, Formal analysis, Investigation, Methodology. **Xinyu Li:** Data curation, Formal analysis, Investigation, Methodology. **Xiaobo Chen:** Writing – review & editing.

## Declaration of competing interest

The authors declare that they have no known competing financial interests or personal relationships that could have appeared to influence the work reported in this paper.

## Acknowledgments

This work has been financially supported by the National Natural Science Foundation of China (U1809214), the Natural Science Foundation of Zhejiang Province (LY20E080014), and the Science and Technology Project of Zhoushan City (2022C41011).

## Appendix A. Supplementary data

Supplementary data to this article can be found online at https://doi.org/10.1016/j.esci.2023.100208.

## References

[1] H. Xu, Y. Jia, Z. Sun, J. Su, Q.S. Liu, Q. Zhou, G. Jiang, Environmental pollution, a hidden culprit for health issues, Eco-Environ. Health 1 (2022) 31–45.
[2] A. Previšić*, M. Vilenica, N. Vučković, M. Petrović, M. Rožman, Aquatic insects transfer pharmaceuticals and endocrine disruptors from aquatic to terrestrial ecosystems, Environ. Sci. Technol. 55 (2021) 3736–3746.
[3] S. Feijoo, M. Kamali, R. Dewil, A review of wastewater treatment technologies for the degradation of pharmaceutically active compounds: carbamazepine as a case study, Chem. Eng. J. 455 (2023) 140589.
[4] Y. Liu, K. Wang, Z. Zhou, X. Wei, S. Xia, X. Wang, Y.F. Xie, X. Huang, Boosting the performance of nanofiltration membranes in removing organic micropollutants: trade-off effect, strategy evaluation, and prospective development, Environ. Sci. Technol. 56 (2022) 15220–15237.
[5] D. Wang, M.A. Mueses, J.A.C. Márquez, F. Machuca-Martínez, I. Grčić, R.P.M. Moreira, G.L. Puma, Engineering and modeling perspectives on photocatalytic reactors for water treatment, Water Res. 202 (2021) 117421.
[6] P. Zhou, M. Luo, S. Guo, Optimizing the semiconductor-metal-single-atom interaction for photocatalytic reactivity, Nat. Rev. Chem. 6 (2022) 823–838.
[7] M. Caban, P. Stepnowski, How to decrease pharmaceuticals in the environment? A review, Environ. Chem. Lett. 19 (2021) 3115–3138.
[8] W. Zhao, W. Chen, F. Huang, Toward large-scale water treatment using nanomaterials, Nano Today 27 (2019) 11–27.
[9] L. Jing, W. Zhou, G. Tian, H. Fu, Surface tuning for oxide-based nanomaterials as efficient photocatalysts, Chem. Soc. Rev. 42 (2013) 9509–9549.
[10] D. Zhou, H. Luo, F. Zhang, J. Wu, J. Yang, H. Wang, Efficient photocatalytic degradation of the persistent PET fiber-based microplastics over Pt nanoparticles decorated N-doped $TiO_2$ nanoflowers, Adv. Fiber Mater. 4 (2022) 1094–1107.

[11] C. Wang, K. Liu, D. Wang, G. Wang, P.K. Chu, Z. Meng, X. Wang, Hierarchical CuO-ZnO/$SiO_2$ fibrous membranes for efficient removal of Congo red and 4-nitrophenol from water, Adv. Fiber Mater. 4 (2022) 1069–1080.

[12] S. Li, Y. Li, Y. Shao, H. Wang, Emerging two-dimensional materials constructed nanofluidic fiber: properties, preparation and applications, Adv. Fiber Mater. 4 (2022) 129–144.

[13] X. Sun, L. Li, S. Jin, W. Shao, H. Wang, X. Zhang, Y. Xie, Interface boosted highly efficient selective photooxidation in $Bi_3O_4Br/Bi_2O_3$ heterojunctions, eScience 3 (2023) 100095.

[14] S. Bai, H. Qiu, M. Song, G. He, F. Wang, Y. Liu, L. Guo, Porous fixed-bed photoreactor for boosting C-C coupling in photocatalytic $CO_2$ reduction, eScience 2 (2022) 428–437.

[15] H. Yang, C. Li, T. Liu, T. Fellowes, S.Y. Chong, L. Catalano, M. Bahri, W. Zhang, Y. Xu, L. Liu, W. Zhao, A.M. Gardner, R. Clowes, N.D. Browning, X. Li, A.J. Cowan, A.I. Cooper, Packing-induced selectivity switching in molecular nanoparticle photocatalysts for hydrogen and hydrogen peroxide production, Nat. Nanotechnol. 18 (2023) 307–315.

[16] Q. Wang, C. Pornrungroj, S. Linley, E. Reisner, Strategies to improve light utilization in solar fuel synthesis, Nat, Energy 7 (2022) 13–24.

[17] E. Swift, A durable semiconductor photocatalyst, Science 365 (2019) 320–321.

[18] P. Raizada, A. Sudhaik, S. Patial, V. Hasija, A.A.P. Khan, P. Singh, S. Gautam, M. Kaur, V.-H. Nguyen, Engineering nanostructures of CuO-based photocatalysts for water treatment: current progress and future challenges, Arab. J. Chem. 13 (2020) 8424–8457.

[19] A. Chawla, A. Sudhaik, Sonu, P. Raizada, T. Ahamad, Q.V. Le, V.-H. Nguyen, S. Thakur, A.K. Mishra, R. Selvasembian, P. Singh, Bi-rich $Bi_xO_yBr_z$-based photocatalysts for energy conversion and environmental remediation: a review, Coord. Chem. Rev. 491 (2023) 215246.

[20] Z. Pan, M. Zhao, H. Zhuzhang, G. Zhang, M. Anpo, X. Wang, Gradient Zn-doped poly heptazine imides integrated with a van der Waals homojunction boosting visible light-driven water oxidation activities, ACS Catal. 11 (2021) 13463–13471.

[21] G. Zhang, G. Li, T. Heil, S. Zafeiratos, F. Lai, A. Savateev, M. Antonietti, X. Wang, Tailoring the grain boundary chemistry of polymeric carbon nitride for enhanced solar hydrogen production and $CO_2$ reduction, Angew. Chem. Int. Ed. 58 (2019) 3433–3437.

[22] Q. Wang, G. Zhang, W. Xing, Z. Pan, D. Zheng, S. Wang, Y. Hou, X. Wang, Bottom-up synthesis of single-Crystalline poly (triazine imide) nanosheets for photocatalytic overall water splitting, Angew. Chem. Int. Ed. 62 (2023) e202307930.

[23] V. Selvaraj, W.-J. Ong, A. Pandikumar, Defect engineering of BiOX (X = Cl, Br, I) based photocatalysts for energy and environmental applications: current progress and future perspectives, Coord. Chem. Rev. 464 (2022) 214541.

[24] Z. Luo, X. Ye, S. Zhang, S. Xue, C. Yang, Y. Hou, W. Xing, R. Yu, J. Sun, Z. Yu, X. Wang, Unveiling the charge transfer dynamics steered by built-in electric fields in BiOBr photocatalysts, Nat. Commun. 13 (2022) 2230.

[25] Y. Guo, H. Wen, T. Zhong, H. Huang, Z. Lin, Edge-rich atomic-layered BiOBr quantum dots for photocatalytic molecular oxygen activation, Chem. Eng. J. 445 (2022) 136776.

[26] M. Shi, G. Li, J. Li, X. Jin, X. Tao, Z. Bin, E.A. Pidko, R. Li, C. Li, Intrinsic facet-dependent reactivity of well-defined BiOBr nanosheets on photocatalytic water splitting, Angew. Chem. Int. Ed. 132 (2020) 6652–6657.

[27] Y. Shi, J. Li, D. Huang, X. Wang, Y. Huang, C. Chen, R. Li, Specific adsorption and efficient degradation of cylindrospermopsin on oxygen-vacancy sites of BiOBr, ACS Catal. 13 (2022) 445–458.

[28] X. Li, T. Liu, Y. Zhang, J. Cai, M. He, M. Li, Z. Chen, L. Zhang, Growth of BiOBr/ZIF-67 nanocomposites on carbon fiber cloth as filter-membrane-shaped photocatalyst for degrading pollutants in flowing wastewater, Adv. Fiber Mater. 4 (2022) 1620–1631.

[29] T. Jia, J. Wu, J. Song, Q. Liu, J. Wang, Y. Qi, P. He, X. Qi, L. Yang, P. Zhao, In situ self-growing 3D hierarchical BiOBr/$BiOIO_3$ Z-scheme heterojunction with rich oxygen vacancies and iodine ions as carriers transfer dual-channels for enhanced photocatalytic activity, Chem. Eng. J. 396 (2020) 125258.

[30] S. Vinoth, A. Pandikumar, Ni integrated S-g$C_3N_4$/BiOBr based type-II heterojunction as a durable catalyst for photoelectrochemical water splitting, Renew. Energy 173 (2021) 507–519.

[31] S. Li, Q. Ma, L. Chen, Z. Yang, M. Aqeel Kamran, B. Chen, Hydrochar-mediated photocatalyst $Fe_3O_4$/BiOBr@HC for highly efficient carbamazepine degradation under visible LED light irradiation, Chem. Eng. J. 433 (2022) 134492.

[32] G. Ren, M. Shi, Z. Li, Z. Zhang, X. Meng, Electronic metal-support Interaction via defective-induced platinum modified BiOBr for photocatalytic $N_2$ fixation, Appl. Catal. B 327 (2023) 122462.

[33] S. Nishioka, K. Hojo, L. Xiao, T. Gao, Y. Miseki, S. Yasuda, T. Yokoi, K. Sayama, T.E. Mallouk, K. Maeda, Surface-modified, dye-sensitized niobate nanosheets enabling an efficient solar-driven Z-scheme for overall water splitting, Sci. Adv. 8 (2022) eadc9115.

[34] P. Raizada, A. Sudhaik, P. Singh, P. Shandilya, A.K. Saini, V.K. Gupta, J.-H. Lim, H. Jung, A. Hosseini-Bandegharaei, Fabrication of $Ag_3VO_4$ decorated phosphorus and sulphur co-doped graphitic carbon nitride as a high-dispersed photocatalyst for phenol mineralization and E. coli disinfection, Sep. Purif. Technol. 212 (2019) 887–900.

[35] P. Raizada, A. Sudhaik, P. Singh, P. Shandilya, V.K. Gupta, A. Hosseini-Bandegharaei, S. Agrawal, $Ag_3PO_4$ modified phosphorus and sulphur co-doped graphitic carbon nitride as a direct Z-scheme photocatalyst for 2, 4-dimethyl phenol degradation, J. Photochem. Photobiol. A 374 (2019) 22–35.

[36] P. Raizada, A. Sudhaik, P. Singh, A. Hosseini-Bandegharaei, P. Thakur, Converting type II AgBr/VO into ternary Z scheme photocatalyst via coupling with phosphorus doped g-$C_3N_4$ for enhanced photocatalytic activity, Sep. Purif. Technol. 227 (2019) 115692.

[37] X. Ma, H. Lin, Y. Li, L. Wang, X. Pu, Y. Xi, Dramatically enhanced visible-light-responsive $H_2$ evolution of $Cd_{1-x}Zn_xS$ via the synergistic effect of $Ni_2P$ and 1T/2H $MoS_2$ cocatalysts, Chin. J. Struct. Chem. 40 (2022) 7–22.

[38] S. Li, M. Cai, C. Wang, Y. Liu, $Ta_3N_5$/CdS core-shell S-scheme heterojunction nanofibers for efficient photocatalytic removal of antibiotic tetracycline and Cr(VI): performance and mechanism insights, Adv. Fiber Mater. 5 (2023) 994–1007.

[39] S. Li, M. Cai, Y. Liu, C. Wang, K. Lv, X. Chen, S-scheme photocatalyst TaON/$Bi_2WO_6$ nanofibers with oxygen vacancies for efficient abatement of antibiotics and Cr(VI): intermediate eco-toxicity analysis and mechanistic insights, Chin. J. Catal. 43 (2022) 2652–2664.

[40] L. Zhang, J. Zhang, H. Yu, J. Yu, Emerging S-scheme photocatalyst, Adv. Mater. 34 (2022) 2107668.

[41] S. Liu, K. Wang, M. Yang, Z. Jin, Rationally designed $Mn_{0.2}Cd_{0.8}S$@CoAl LDH S-scheme heterojunction for efficient photocatalytic hydrogen production, Acta Phys. Chim. Sin. 38 (2022) 2109023.

[42] M. Cai, Y. Liu, K. Dong, X. Chen, S. Li, Floatable S-scheme $Bi_2WO_6/C_3N_4$/carbon fiber cloth composite photocatalyst for efficient water decontamination, Chin. J. Catal. 52 (2023) 239–251.

[43] Z. Miao, Q. Wang, Y. Zhang, L. Meng, X. Wang, In situ construction of S-scheme AgBr/BiOBr heterojunction with surface oxygen vacancy for boosting photocatalytic $CO_2$ reduction with $H_2O$, Appl. Catal. B 301 (2022) 120802.

[44] N. Chen, X. Jia, H. He, H. Lin, M. Guo, J. Cao, J. Zhang, S. Chen, Promoting photocarriers separation in S-scheme system with $Ni_2P$ electron bridge: the case study of BiOBr/$Ni_2P$/g-$C_3N_4$, Chin. J. Catal. 43 (2022) 276–287.

[45] S. Navalón, A. Dhakshinamoorthy, M. Álvaro, B. Ferrer, H. García, Metal-organic frameworks as photocatalysts for solar-driven overall water splitting, Chem. Rev. 123 (2023) 445–490.

[46] K. Wang, Y. Li, L.-H. Xie, X. Li, J.-R. Li, Construction and application of base-stable MOFs: a critical review, Chem. Soc. Rev. 51 (2022) 6417–6441.

[47] P.M. Stanley, J. Haimerl, N.B. Shustova, R.A. Fischer, J. Warnan, Merging molecular catalysts and metal-organic frameworks for photocatalytic fuel production, Nat. Chem. 14 (2022) 1342–1356.

[48] X. Liu, Y. Zhang, X. Guo, H. Pang, Electrospun metal-organic framework nanofiber membranes for energy storage and environmental protection, Adv. Fiber Mater. 4 (2022) 1463–1485.

[49] R. Freund, O. Zaremba, G. Arnauts, R. Ameloot, G. Skorupskii, M. Dincă, A. Bavykina, J. Gascon, A. Ejsmont, J. Goscianska, M. Kalmutzki, U. Lächelt, E. Ploetz, C.S. Diercks, S. Wuttke, The current status of MOF and COF applications, Angew. Chem. Int. Ed. 60 (2021) 23975–24001.

[50] Q. Zhao, X.-H. Yi, C.-C. Wang, P. Wang, W. Zheng, Photocatalytic Cr(VI) reduction over MIL-101(Fe)–$NH_2$ immobilized on alumina substrate: from batch test to continuous operation, Chem. Eng. J. 429 (2022) 132497.

[51] N. Liu, M. Tang, J. Wu, L. Tang, W. Huang, Q. Li, J. Lei, X. Zhang, L. Wang, Boosting visible-light photocatalytic performance for $CO_2$ reduction via hydroxylated graphene quantum dots sensitized MIL-101(Fe), Adv. Mater. Interfac. 7 (2020) 2000468.

[52] F. Zhao, Y. Liu, S.B. Hammouda, B. Doshi, N. Guijarro, X. Min, C.-J. Tang, M. Sillanpää, K. Sivula, S. Wang, MIL-101(Fe)/g-$C_3N_4$ for enhanced visible-light-driven photocatalysis toward simultaneous reduction of Cr(VI) and oxidation of bisphenol A in aqueous media, Appl. Catal. B 272 (2020) 119033.

[53] Z. Jiang, X. Xu, Y. Ma, H.S. Cho, D. Ding, C. Wang, J. Wu, P. Oleynikov, M. Jia, J. Cheng, Y. Zhou, O. Terasaki, T. Peng, L. Zan, H. Deng, Filling metal-organic framework mesopores with $TiO_2$ for $CO_2$ photoreduction, Nature 586 (2020) 549–554.

[54] J. Xu, Y. Qi, C. Wang, L. Wang, $NH_2$-MIL-101(Fe)/Ni(OH)$_2$-derived C,N-codoped $Fe_2P/Ni_2P$ cocatalyst modified g-$C_3N_4$ for enhanced photocatalytic hydrogen evolution from water splitting, Appl. Catal. B 241 (2019) 178–186.

[55] P. Jiménez-Calvo, V. Caps, M.N. Ghazzal, C. Colbeau-Justin, V.K. Keller, Au/$TiO_2(P_{25})$-g$C_3N_4$ composites with low g$C_3N_4$ content enhance $TiO_2$ sensitization for remarkable $H_2$ production from water under visible-light irradiation, Nano Energy 75 (2020) 104888.

[56] D. Liu, C. Xue, Plasmonic coupling architectures for enhanced photocatalysis, Adv. Mater. 33 (2021) 2005738.

[57] H. Sheng, J. Wang, J. Huang, Z. Li, G. Ren, L. Zhang, L. Yu, M. Zhao, X. Li, G. Li, N. Wang, C. Shen, G. Lu, Strong synergy between gold nanoparticles and cobalt porphyrin induces highly efficient photocatalytic hydrogen evolution, Nat. Commun. 14 (2023) 1528.

[58] M. Wang, Y. Tang, Y. Jin, Modulating Catalytic performance of metal-organic framework composites by localized surface plasmon resonance, ACS Catal. 9 (2019) 11502–11514.

[59] S. Han, B. Li, L. Huang, H. Xi, Z. Ding, J. Long, Construction of $ZnIn_2S_4$-$CdIn_2S_4$ microspheres for efficient photo-catalytic reduction of $CO_2$ with visible light, Chin. J. Struct. Chem. 41 (2022) 2201007–2201013.

[60] W.-Y. Xu, C. Li, F.-L. Li, J.-Y. Xue, W. Zhang, H. Gu, B.F. Abrahams, J.-P. Lang, A hybrid catalyst for efficient electrochemical $N_2$ fixation formed by decorating amorphous $MoS_3$ nanosheets with MIL-101(Fe) nanodots, Sci. China Chem. 65 (2022) 885–891.

[61] R. Ning, H. Pang, Z. Yan, Z. Lu, Q. Wang, Z. Wu, W. Dai, L. Liu, Z. Li, G. Fan, X. Fu, An innovative S-scheme AgCl/MIL-100(Fe) heterojunction for visible-light-driven degradation of sulfamethazine and mechanism insight, J. Hazard Mater. 435 (2022) 129061.

[62] S. Li, M. Cai, Y. Liu, C. Wang, R. Yan, X. Chen, Constructing $Cd_{0.5}Zn_{0.5}S/Bi_2WO_6$ S-scheme heterojunction for boosted photocatalytic antibiotic oxidation and Cr(VI) reduction, Adv. Powder Mater. 2 (2023) 100073.

[63] H. Gong, L. Wang, K. Zhou, D. Zhang, Y. Zhang, V. Adamaki, C. Bowen, A. Sergejevs, Improved photocatalytic performance of gradient reduced $TiO_2$ ceramics with aligned pore channels, Adv. Powder Mater. 1 (2022) 100025.
[64] S. Huo, W. Gao, P. Zhou, Z. Deng, Z. Han, X. Cui, X. Lu, Magnetic porous carbon composites for rapid and highly efficient degradation of organic pollutants in water, Adv. Powder Mater. 1 (2022) 100028.
[65] C. Liu, P. Wang, Y. Qiao, G. Zhou, Self-assembled $Bi_2SeO_5$/rGO/MIL-88A Z-scheme heterojunction boosting carrier separation for simultaneous removal of Cr (VI) and chloramphenicol, Chem. Eng. J. 431 (2021) 133289.
[66] Q. Huang, J. Hu, Y. Hu, J. Liu, J. He, G. Zhou, N. Hu, Z. Yang, Y. Zhang, Y. Zhou, Z. Zou, Simultaneously enhanced photocatalytic cleanup of Cr(vi) and tetracycline via a $ZnIn_2S_4$ nanoflake-decorated 24-faceted concave MIL-88B(Fe) polyhedron S-scheme system, Environ. Sci. Nano 9 (2022) 4433–4444.
[67] K. Gelderman, L. Lee, S.W. Donne, Flat-band potential of a semiconductor: using the Mott-Schottky equation, J. Chem. Educ. 84 (2007) 685.
[68] G. Han, F. Xu, B. Cheng, Y. Li, J. Yu, L. Zhang, Enhanced photocatalytic $H_2O_2$ production over inverse opal ZnO@polydopamine S-scheme heterojunctions, Acta Phys. Chim. Sin. 38 (2022) 2112037.
[69] Z. Wang, E. Almatrafi, H. Wang, H. Qin, W. Wang, L. Du, S. Chen, G. Zeng, P. Xu, Cobalt single atoms anchored on oxygen-doped tubular carbon nitride for efficient peroxymonosulfate activation: simultaneous coordination structure and morphology modulation, Angew. Chem. Int. Ed. 134 (2022) e202202338.
[70] N. Zhao, J. Peng, J. Wang, M. Zhai, Novel carboxy-functionalized PVP-CdS nanopopcorns with homojunctions for enhanced photocatalytic hydrogen evolution, Acta Phys. Chim. Sin. 38 (2022) 2004046.
[71] A. Hu, J.J. Guo, H. Pan, Z. Zuo, Selective functionalization of methane, ethane, and higher alkanes by cerium photocatalysis, Science 361 (2018) 668–672.
[72] A. Kumar, P. Choudhary, A. Kumar, P.H. Camargo, V. Krishnan, Recent advances in plasmonic photocatalysis based on $TiO_2$ and noble metal nanoparticles for energy conversion, environmental remediation, and organic synthesis, Small 18 (2021) 2101638.
[73] V. Gupta, S. Sarkar, O. Aftenieva, T. Tsuda, L. Kumar, D. Schletz, J. Schultz, A. Kiriy, A. Fery, N. Vogel, T.A.F. König, Nanoimprint lithography facilitated plasmonic-photonic coupling for enhanced photoconductivity and photocatalysis, Adv. Funct. Mater. 31 (2021) 2105054.